Available online at www.sciencedirect.com
SCIENCE DIRECT
Tectonophysics 413 (2006) 109–125
TECTONOPHYSICS
www.elsevier.com/locate/tecto

Stress transfer in earthquakes, hazard estimation and ensemble forecasting: Inferences from numerical simulations

John B. Rundle [a,*], Paul B. Rundle [b,c,1], Andrea Donnellan [d,2], P. Li [d], W. Klein [e,3], Gleb Morein [f,4], D.L. Turcotte [g,5], Lisa Grant [h,6]

[a] *Center for Computational Science and Engineering, The University of California, One Shields Ave., Davis, CA, 95616, United States*
[b] *Center for Computational Science and Engineering, The University of California, One Shields Ave., Davis, CA, 95616; United States*
[c] *Department of Physics, Harvey Mudd College, Claremont, CA, 91711, United States*
[d] *Division of Earth and Space Science, Jet Propulsion Laboratory, Pasadena, CA 91125, United States*
[e] *Department of Physics, Boston University, Boston, MA, United States*
[f] *Center for Computational Science and Engineering, The University of California, One Shields Ave., Davis, CA, 95616, United States*
[g] *Department of Geology, The University of California, One Shields Ave., Davis, CA, 95616, United States*
[h] *Department of Environmental Health, Safety and Policy, The University of California, Irvine, CA, 92697-7070, United States*

Received 19 November 2004; received in revised form 31 May 2005; accepted 4 October 2005

Abstract

Observations indicate that earthquake faults occur in topologically complex, multi-scale networks driven by plate tectonic forces. We present realistic numerical simulations, involving data-mining, pattern recognition, theoretical analyses and ensemble forecasting techniques, to understand how the observable space–time earthquake patterns are related to the fundamentally inaccessible and unobservable dynamics. Numerical simulations can also help us to understand how the different scales involved in earthquake physics interact and influence the resulting dynamics. Our simulations indicate that elastic interactions (stress transfer) combined with the nonlinearity in the frictional failure threshold law lead to the self-organization of the statistical dynamics, producing 1) statistical distributions for magnitudes and frequencies of earthquakes that have characteristics similar to those possessed by the Gutenberg–Richter magnitude–frequency distributions observed in nature; and 2) clear examples of stress transfer among fault activity described by stress shadows, in which an earthquake on one group of faults reduces the Coulomb failure stress on other faults, thereby delaying activity on those faults. In this paper, we describe the current state of modeling and simulation efforts for *Virtual California*, a model for all the major active strike slip faults in California. Noting that the Working Group on California Earthquake Probabilities (WGCEP) uses statistical distributions to produce earthquake forecast probabilities, we demonstrate that *Virtual California* provides a powerful tool for testing the applicability and reliability of the WGCEP statistical methods. Furthermore, we show how the simulations can be used to develop statistical earthquake forecasting techniques that are

* Corresponding author. Tel.: +1 530 752 6462.
E-mail addresses: jbrundle@ucdavis.edu (J.B. Rundle), prundle@ucdavis.edu (P.B. Rundle), andrea.donnellan@jpl.nasa.gov (A. Donnellan), klein@buphy.bu.edu (W. Klein), gleb@cse.ucdavis.edu (G. Morein), turcotte@geology.ucdavis.edu (D.L. Turcotte), lgrant@uci.edu (L. Grant).
[1] Tel.: +1 530 752 6419.
[2] Tel.: +1 818 354 4737.
[3] Tel.: +1 617 353 2188.
[4] Tel.: +1 530 752 6419.
[5] Tel.: +1 530 752 6808.
[6] Tel.: +1 949 824 5491.

0040-1951/$ - see front matter
doi:10.1016/j.tecto.2005.10.031

complementary to the methods used by the WGCEP, but improve upon those methods in a number of important ways. In doing so, we distinguish between the "official" forecasts of the WGCEP, and the "research-quality" forecasts that we discuss here. Finally, we provide a brief discussion of future problems and issues related to the development of ensemble earthquake hazard estimation and forecasting techniques.

Keywords: Earthquakes; Numerical simulations; Virtual California

1. Introduction

Geologic observations indicate that earthquake faults occur in topologically complex, multi-scale networks that are driven to failure by external forces arising from plate tectonic motions (Turcotte, 1991; Rundle, 1988; Rundle et al., 2000a,b, 2001; Hashimoto, 2001; Ward, 1996, 2000; Hashimoto and Matsu'ura, 2002). The earthquakes that occur on these fault systems represent a complex, high-dimensional nonlinear dynamical system (Turcotte, 1991; Hergarten, 2002; Rundle et al., 2003), characterized by a rich spectrum of properties, including interacting fault segments, strongly nonlinear friction, and noise. Forecasting and prediction of the future evolution and activity in such complex dynamical systems are known to be extremely difficult, even when the fundamental dynamical variables are observable (Kravtsov and Kadtke, 1996).

There are two serious drawbacks to a purely observational approach to the problem of earthquake forecasting: 1) Inaccessible and unobservable stress–strain dynamics that are obscurely related to the observable and accessible space–time patterns of earthquakes that are observed, and 2) strongly multi-scale dynamics that cover a vast range of space and time scales (Turcotte, 1991; Rundle et al., 2003). These problems are illustrated, for example, by considering the World Stress Map (WSM: Zoback, 1992), where point values of static time-averaged estimates of maximum and minimum principal stresses in space are given. Since to define the fault dynamics, one needs dynamic stresses and strains for all space and time, the WSM data, although the best current data on this parameter, are not sufficient for this purpose.

The method used by the United States Geological Survey Working Group on California Earthquake Probabilities[7] (WGCEP, 2003) is a complex, consensus-based process that uses observational data describing earthquake slips, lengths, creep rates and other information on regional faults as inputs to a San Francisco Bay Regional fault model. The statistical properties of the model are determined through the assumption of a probability distribution describing the inter-event statistics of rupture on geological fault segments. In their most recent study[7] the WGCEP (2003) utilized the Brownian passage time probability distribution (also known as an inverse Gaussian distribution). The mean and standard deviations of the distributions for event times on the fault segments were constrained by geological and seismological observations. Using their forecast algorithm, the WGCEP (2003) found that for earthquakes having $M \geq 6.7$ during the 30 year period 2002–2031 is 18.2%. Earlier studies by the WGCEP tended to favor the use of the Log Normal distribution.

The use of numerical simulations, together with theory and analysis, can be a useful tool for relating the unobservable dynamics to the observable patterns for purposes of earthquake forecasting and prediction. Moreover, topologically and dynamically realistic simulations allow the fundamental assumptions of involved with the WGCEP method to be tested in a realistic virtual environment (numerical laboratory). Simulations also have the advantage that the probability distribution for inter-earthquake time intervals can be measured from simulation data. These measured distributions can then be examined for clues to the form of the distribution(s) appropriate for use in applying the WGCEP forecasting methods.

The construction of such models (Ward, 2000; Rundle et al., 2001) involves not only modern computational algorithms and resources, but in addition, many types of earthquake-related data, including seismic, geodetic, paleoseismic, and laboratory rock mechanics experiments to constrain the parameters required. The data are used both to determine physical properties of the models we simulate, a process of data assimilation, as well as to critically test the results of our simulation-derived forecasts, so that future forecasts and predictions can be developed. Similar to the General Circulation Models (GCMs) that are used in weather and climate forecasting (Covey et al., 2003; Achuta Rao

[7] WGCEP Study http://quake.wr.usgs.gov/research/seismology/wg02.

and Sperber, 2002), the construction of earthquake simulation models can be regarded as a community-wide activity that integrates the existing knowledge into a predictive, system-level framework.

Models will always include idealizations of nature. The idea is to focus on particular physical processes to be understood, and to introduce a hierarchy of models with increasingly complexity, and then to understand the influence of each level of complexity on the emergent collective dynamics at successively more detailed levels. For example, Crampin and Chastin (2003) and Crampin and Peacock (2005) have pointed out that critical systems of cracks may lead to anisotropic long range interactions, and stochastic processes on a large range of physical scales. In order to understand the effect of such critical crack systems, one must first consider dynamical models *without* each of these components, so that their influence can be properly evaluated by comparison to successively more complex models.

Other factors that must be considered in the construction of earthquake fault system simulations used for the purposes of either validating WGCEP methods or measurement of probability distributions have been discussed extensively by Mulargia (1997, 2001), and Mulargia (2004). For example, prior to the deployment of "officially endorsed" forecasts (as opposed to the "research-quality" forecasts discussed here), a validation process must be designed and implemented to build confidence in the ensemble of simulations used (Mulargia, 1997, 2001). In addition, issues of catalog completeness of the events used in the validation process are equally important (Mulargia and Tinti, 1985).

There are major differences between the simulation-based forecasts given in this paper (research-quality forecasts), and the officially endorsed statistical forecasts given by the WGCEP (2003). In our approach, it is not necessary to prescribe a probability distribution of inter-event times. The distribution of event intervals is obtained directly from our simulations, which include the physics of fault interactions and dynamics. Since both methods use the same database for mean fault slip on fault segments, they give approximately equal mean inter-event times. The major difference between the two methods lies in the way in which inter-event times and probabilities for joint failure of multiple segments are computed. In our simulation approach, these times and probabilities come from the modeling of fault interactions through the inclusion of basic dynamical processes in a topologically realistic model. In the WGCEP (2003) statistical approach, times and probabilities are embedded in the choice of an applicable probability distribution function, as well as choices associated with a variety of other statistical weighting factors describing joint probabilities for multi-segment events.

Finally, the strong coupling of earthquake dynamics across a vast range of spatial and temporal scales that are both much smaller and much larger than "human" dimensions [8,9,10,11] (Mora, 1999; Matsu'ura et al., 2001) is a major motivation for pursuing a simulation-based approach to understanding and forecasting earthquakes. The important spatial scales span the range from the *grain scale*, of 1 nm to 1 cm; the *fault zone scale*, at 1 cm to 100 m; the *fault segment scale*, at 100 m to 10 km; the *fault system or network scale*, at 10 to 1000 km; finally to the *tectonic plate boundary scale* in excess of 1000 km. Important time scales span the range from the *source process time scale* of fractions of seconds to seconds; to the *stress transfer scale* of seconds to years; to *event recurrence time scales* of years to many thousands of years; finally to the *fault topology evolution scale*, in excess of many thousands of years up to millions of years. There is considerable evidence that many/most/all of these spatial and temporal scales are strongly coupled by the dynamics. Consider, as evidence, the Gutenberg–Richter relation, which is equivalent to a power law dependence of the frequency of events on event size. Power laws are a fundamental property of scale-invariant, self-organizing systems whose dynamics and structures are strongly coupled and correlated across many scales in space and time. If the dynamics were uncorrelated or random, one would expect to see Gaussian or Poissonian statistics. This fact, in conjunction with the underlying dynamics are associated with stress transfer over a variety of scales, suggests that earthquake fault systems are also spatiotemporally correlated over a range of scales.

Numerical simulations can help us to understand how processes operating on time scales of seconds and spatial scales of meters, such as source process times in fault zones, influence processes that are observed to occur over time scales of hundreds of years and spatial scales of hundreds of kilometers, such as recurrence of great earthquakes. Numerical simulations

[8] QuakeSim home page, http://www-aig.jpl.nasa.gov/public/dus/quakesim/.

[9] ACES home page, http://quakes.earth.uq.edu.au/ACES.

[10] SCEC home page, Southern California Earthquake Center, http://www.scec.org/.

[11] Earthscope home page, http://www.earthscope.org/.

also allow us to connect observable surface data to underlying unobservable stress–strain dynamics, so we can determine how these are related. Thus we conclude that numerical simulations are essential if we are to understand the physics of earthquake fault systems.

We have written this paper in such a way that the reader may skip the mathematics in Sections 2 and 3 without penalty, and instead proceed directly to Sections 4 and 5, which discuss the important results of the paper. The casual reader may in fact simply examine the figures, whose captions are detailed enough to bring out the main results.

More specifically, Section 2 discusses the system-level physics of the current version of the Virtual California earthquake fault model. Note that the major simulation and analysis codes used in this paper are open-source codes that can be found at the QuakeSim web site.[8] The following Section 3 describes how existing earthquake data on fault offset rates and slips due to historic events are assimilated into the model using a "static" data assimilation technique. Section 4 then gives a selection of results from the simulations, including data on magnitude–frequency of events, as well as synoptic views of the Coulomb Failure Function (CFF) in space and time through many earthquake cycles that clearly show examples of stress transfer and stress shadows. Section 5 describes and extends the methodology of the Working Group on California Earthquake Probabilities (WGCEP, 2003) using the Virtual California model and shows that results are generally consistent with forecasts made using the existing methodology. Section 6 contains final comments and a discussion.

2. System-level physics of Virtual California model

Although all scales are important, we place more emphasis on the *fault system* or *fault network* scale, since this is the scale of most current and planned observational data networks. It is also the scale upon which the data we are interested in understanding large and great earthquakes are collected. Furthermore, since it is not possible to uniquely determine the stress distribution on the southern California fault system, and since the friction laws and elastic stress transfer moduli are not well known, it makes little sense to pursue a deterministic computational model of the space–time evolution of stress on the fault system.

We therefore use a quasi-static approach in which the dynamics of rupture are neglected. Slip is applied to all fault segments until a segment reaches the failure threshold. The segment is then allowed to slip. The elastic stresses caused by this slip are then transferred to all other fault segments using the classic Green's function approach. This stress transfer will often induce secondary failures, some on other segments connected to the initial fault segment, and some on other segments that are unconnected to the initial segment. If the stress transfer results in stresses that exceed the applicable failure thresholds, further failures are considered in sequence. This approach is basically a long range (mean field) cellular automaton in that slip events are separated in space and time and considered individually, but the resulting stress transfer is long range, as contrasted with nearest-neighbor stress transfer.

Computational and theoretical work (Preston, 2001; Preston et al., 2005) have shown that for systems such as earthquake fault systems, the final state of slip after the earthquake is independent of the order in which the sites fail. Models of this type are called "Abelian" (Gabrielov et al., 1994). For such models, the results obtained, particularly for statistical distributions, are insensitive to the cellular automaton dynamics used. Nevertheless, we approximate the triggering effect on slip due to wave-mediated stress transfer by the use of a simple representation of a dynamic stress intensity factor, as we discuss below.

The Virtual California model (Rundle et al., 2000a,b, 2001) is a stochastic, cellular automaton application of an earthquake *backslip* model, in that loading of each fault segment occurs via the accumulation of slip deficit $\phi(\boldsymbol{x},t)=s(\boldsymbol{x},t)-Vt$, where $s(\boldsymbol{x},t)$ is slip, V is long term slip rate, and t is time. For completeness, we provide a summary of the major characteristics of the Virtual California model. Note that these codes are available via open-source.[8]

1. *Surfaces of discontinuity* (faults) on which slip occurs at the time of an earthquake, and which are subject to frictional resistance. Here we restrict the model to topologically complex systems of vertically dipping faults mirroring the complexity found on the natural fault networks of California.
2. *Stochastic dynamics*. We are interested in the space–time patterns and correlations that emerge from the underlying stress–strain dynamics. These correlations evolve over hundreds to thousands of years, time scales much longer than the time scales associated either with rupture and elastic wave propagation. Most of the elastic and frictional parameters for faults and earth materials, although known in the laboratory, remain poorly defined in nature. For this reason, it makes little sense to attempt a determinis-

tic solution to the equations of motion. Instead, we use a Cellular Automaton (CA) approach, in which the dynamics are parameterized by random variables chosen from well defined probability distributions. The stochastic nature of the dynamics is implemented during the sliding process of a fault segment to reduce its stress, in which a random overshoot or undershoot of up to $\pm 10\%$ is added. The density function characterizing the overshoot–undershoot is a uniform probability density function.

3. *Linear elastic stress transfer* between fault segments. We use quasi-static isotropic stress interaction (Green's function) tensors $T_{ij}^{kl}(\boldsymbol{x}-\boldsymbol{x}')$, which we will write henceforth schematically as $T(\boldsymbol{x}-\boldsymbol{x}')$. Recall that more advanced models may require anisotropic stress interactions (Crampin and Chastin, 2003; Crampin and Peacock, 2005).
4. *Increase of stress* on a fault segment due to plate tectonic forcing parameterized via the backslip method. This method has the advantage that it matches the long term rate of offset V in model faults with the geologically known long term slip rate on faults in nature. Stress increase occurs via the following physics. The stress tensor $\sigma_{ij}(\boldsymbol{x},t)$ is related to the slip $s_l(\boldsymbol{x},t)$ by:

$$\sigma_{ij}(\boldsymbol{x},t) = \int \mathrm{d}\boldsymbol{x}_k T_{ij}^{kl}(\boldsymbol{x}-\boldsymbol{x}')s_l(\boldsymbol{x}',t) \tag{1}$$

Now if $\boldsymbol{x}=\boldsymbol{x}'$, a positive slip $s_l(\boldsymbol{x},t)>0$ results in a *decrease* in stress, $\Delta\sigma_{ij}(\boldsymbol{x},t)<0$. Therefore, if we write the equation:

$$\sigma_{ij}(\boldsymbol{x},t) = \int \mathrm{d}\boldsymbol{x}_k T_{ij}^{kl}(\boldsymbol{x}-\boldsymbol{x}')\{s_l(\boldsymbol{x}',t) - V_l(\boldsymbol{x}')t\} \tag{2}$$

where $V_l(\boldsymbol{x})t=\langle s_l(\boldsymbol{x},t)\rangle$ is the average long term rate of slip at $\boldsymbol{x}'$ over time interval t, then the second term $-V_l(\boldsymbol{x})t$ leads to an *increase* in the stress, $\Delta\sigma_{ij}(\boldsymbol{x},t)>0$. Therefore the second term is the stress accumulation term.

In applying Eqs. (1) and (2) in our simulations, it should be noted that we use the discrete form of the integrals, although we continue to use the continuous (integral) form of the equations in this paper for notational simplicity. In the discrete form, the continuous fault surface is replaced by a network of 650 rectangular segments, each about 10 km in length along strike, with a uniform depth of 15 km. The stress Greens functions, or stress transfer coefficients for the influence of segment i upon segment j are computed by imposing a unit (1 m) of slip on segment i, then computing the change in "average" shear and normal stress on segment j. "Average" in this sense means that we subdivide segment j into $6\times 6=36$ sub-segments, then we compute the stress change due to slip on segment i on each of these sub-segments, then we average the result.

5. *Parameters for friction laws fault topology* that are determined by assimilating seismic, paleoseismic, geodetic, and other geophysical data from events occurring over the last ~200 years in California (Rundle et al., 2000b, 2001; see below for discussion). Frictional resistance laws (Rabinowicz, 1995) range from the simplest Amontons–Coulomb stick–slip friction, to heuristic laws such as slip- or stress rate dependent weakening laws based on recent laboratory friction (Tullis, 1996). In general, several of the friction laws described above can be written in the following representative form:

$$\begin{aligned}\frac{\partial\sigma}{\partial t} &= K_L V - f(\sigma,V)\\ K_L\frac{\partial s}{\partial t} &= f(\sigma,V)\end{aligned} \tag{3}$$

Here $s(\boldsymbol{x},t)$ is slip at position $\boldsymbol{x}$ and time t, $\sigma(\boldsymbol{x},t)$ is shear stress, K_L is the self-interaction or "stress drop stiffness" and $f[\sigma,V]$ is the *stress dissipation function* (Rundle et al., 2001). For example, the "Amontons" or Coulomb friction law, having a sharp failure threshold, can be written in the form (Eq. (2)) using a Dirac delta function:

$$\frac{\partial s}{\partial t} = \frac{\Delta\sigma}{K_L}\delta(t-t_F) \tag{4}$$

where the stress drop $\Delta\sigma=\sigma-\sigma^{\mathrm{R}}(V)$ and $\sigma^{\mathrm{R}}(V)$ is the velocity-dependent residual stress. For laboratory experiments, K_L is the {machine+sample} stiffness, and for simulations, K_L represents the stiffness of a coarse-grained element of the fault of scale size L. $\delta()$ is the Dirac delta, and t_F is any time at which $\sigma(\boldsymbol{x},t_F)=\sigma^{\mathrm{F}}(V)$. Both σ^{F} and σ^{R} can also be parameterized as functions of the normal stress χ by means of coefficients of static μ_{S} and ("effective") kinetic μ_{K} coefficients of friction, $\sigma^{\mathrm{F}}=\mu_{\mathrm{S}}\chi$, $\sigma^{\mathrm{R}}=\mu_{\mathrm{K}}\chi$. The method for data assimilation used is explained in more detail in Rundle et al. (2000b), and is summarized below.

In recent work (Rundle et al., 2001), we have introduced another parameter α, which allows for stable stress-dependent aseismic sliding. The process described by α is seen in laboratory friction experiments

(Tullis, 1996), and is expressed by a generalization of Eq. (4):

$$\frac{\partial s}{\partial t} = \frac{\Delta\sigma}{K_L}\{\alpha + \delta(t - t_F)\} \tag{5}$$

We found that the parameter α, which can be fixed either through laboratory experiments or through field observations (Tullis, 1996; Deng and Sykes, 1997), acts to smooth the stress field on a fault when $\alpha > 0$, and to roughen the fault stress field when $\alpha < 0$ (Rundle et al., 2001). In Virtual California, the value of α for each segment, α_i, is assigned based upon field observations, since it can be shown that α is equal to the ratio of aseismic slip to total slip (seismic + aseismic) during an average slip cycle on a segment. Also, laboratory observations (Tullis, 1996; Karner and Marone, 2000) indicate that observed values of α are a few percent for sliding of granite on granite, so where no observations exist, we assume that all segments have a minimum value of $\alpha \approx 0.1$.

In the model results that we describe here, we further generalize Eq. (5) to include an additional term which depends on rate of stress increase:

$$\frac{\partial s}{\partial t} = \frac{\Delta\sigma}{K_T}\left\{\alpha + \delta(t - t_F) + \beta\delta\left(\frac{\partial\sigma}{\partial t} - \gamma\right)\right\} \tag{6}$$

Here β is a constant having appropriate units (stress/time^2), γ is a critical ("dynamic") stress rate, and K_T represents the total spring constant, or modulus, associated with a fault segment. The last term can be considered to be parameterization of effects associated with a dynamic stress intensity factor (Kanninen and Popelar, 1985; Freund, 1990; Saxena, 1998). It is known that stress rate effects are important in the process of dynamic fracture, such as might be expected during an earthquake. For example, the stress intensity factor K_I for mode I tensile fracture is thought to be of the form:

$$K_{ID} = K_{ID}\left(\frac{\partial\sigma}{\partial t}, T\right) \tag{7}$$

where T is temperature. More specifically, for a crack propagating at velocity v, it has been proposed that the time dependent dynamic stress intensity factor $K_D(t)$ is of the general form (Kanninen and Popelar, 1985):

$$K_D(t) = k(v)K_D(0) = k(v)K_S \tag{8}$$

where K_S is the static stress intensity factor. While not of the exact form of either Eqs. (7) or (8), Eq. (6) is an expression of the idea that the onset of earthquake sliding depends on the stressing rate through the critical threshold value γ.

In the simulations described below, we implement the physical process described by Eq. (6) in our Virtual California CA simulations as follows. We define the Coulomb Failure Function CFF($\boldsymbol{x}, t$):

$$CFF(\boldsymbol{x}, t) = \sigma(\boldsymbol{x}, t) - \mu_S\chi(\boldsymbol{x}, t) \tag{9}$$

According to the first term in Eq. (6), stable slip can occur with amplitude proportional to α for nonzero $\Delta\sigma$. In addition, according to the second term, unstable failure of a fault always occurs when CFF($\boldsymbol{x}, t$)=0. To implement a failure mechanism in a simple way that demonstrates physics similar to the third term, we allow unstable slip of amplitude:

$$\frac{\Delta\sigma}{K_T} = \frac{\sigma(\boldsymbol{x}, t) - \mu_K\chi(\boldsymbol{x}, t)}{K_T} \tag{10}$$

when the condition:

$$-\frac{\partial}{\partial t}\log\{-CFF(\boldsymbol{x}, t)\} > \frac{\gamma}{\Delta\sigma^F} \tag{11}$$

is met. Here $\Delta\sigma_i^F \equiv (\mu_S - \mu_K)_i\chi(\boldsymbol{x}_i)$. We set:

$$\gamma = \frac{\varepsilon\Delta\sigma^F}{\Delta t} \tag{12}$$

where Δt is the time step in the simulation, and is a chosen parameter $0 < \varepsilon < 1$. For a discrete time step Δt as is used in CA computations, Eq. (11) is implemented as:

$$\frac{CFF(\boldsymbol{x}, t) - CFF(\boldsymbol{x}, t + \delta t)}{CFF(\boldsymbol{x}, t)} > \frac{\gamma\Delta t}{\Delta\sigma^F} \equiv \eta \tag{13}$$

(recall that CFF($\boldsymbol{x}, t$)$\leq$0). In Eq. (13), we interpret δt as being the time since the beginning of the earthquake at time t. Implicitly, it is assumed in Eqs. (6), (11) and (13) that:

$$\gamma \gg \left.\frac{\partial\sigma(\boldsymbol{x}, t)}{\partial t}\right|_{\text{Interseismic}} = -\int d\boldsymbol{x}_k T_{ij}^{kl}(\boldsymbol{x} - \boldsymbol{x}')V_l(\boldsymbol{x}') \tag{14}$$

i.e., that the γ-value for stress-rate triggering is much larger than the stress rate characterizing interseismic stress accumulation.

Finally, we note that the friction law Eq. (6) is similar in a number of respects to the three stage process of failure proposed in the model by Mulargia (2004). In their model, stage I is a stick–slip process similar to the second term on the right hand side of Eq. (6). Stage III is essentially a stress rate-dependent process, rather than a stress threshold process, similar to the physics described by the third term in Eq. (6). Since our approach neglects wave propagation, there is no equivalent in Eq. (6) to the stage II process of Mulargia (2004). Also, the stress-dependent aseismic slip exemplified by the first term on the right side of Eq. (6), which is included based on the laboratory experiments of Tullis (1996), has no equivalent in the model of Mulargia (2004).

As described above, the Virtual California simulation uses a cellular automaton (CA) algorithm to update the stress field in response to the steadily increasing stress due to the "backslip" on the faults. Because Eq. (1) represents a *decrease* in stress at $\boldsymbol{x}$ in response to slip at $\boldsymbol{x}'$, the part of Eq. (2) defined by

$$\sigma_{ij}(\boldsymbol{x},t) = -\int \mathrm{d}\boldsymbol{x}_k T_{ij}^{kl}(\boldsymbol{x}-\boldsymbol{x}')V_l(\boldsymbol{x}')t \tag{15}$$

represents an increase in stress at $\boldsymbol{x}$ in response to the long term (plate tectonic) loading $V_l(\boldsymbol{x})t$. In the CA approach, the code steps through time t in steps of size Δt on the *loading time scale*. We choose these time steps to be "small" but exactly how small depends to some extent on the application of interest. Usually, we use time steps $\Delta t = 1$ year, but we can modify the size of the time step for those cases in which we want to be very sure that there is a high probability of having at most 1 earthquake on each time step (rather than 2 or 3, for example). To make this property more transparent, we keep count of the average number of *initiator sites*, i.e., sites having $\mathrm{CFF}(\boldsymbol{x},t) \geq 0$ just after a time update step Δt has been applied, and also the number of such sites on that time step. With a sample simulation, we can judge how small to fix Δt so that, with 95% confidence, there will be only one initiator (thus only one earthquake) per time step. For example, to tabulate the Gutenberg–Richter statistics shown below, we used $\Delta t = .2$ year. By contrast, for $\Delta t = 1$ year, which is a time step we typically use in general stress evolution analyses, we find that there is roughly 1 initiator site per time step with roughly 66% confidence. Note that, during these loading time steps, a small amount of stable slip $\Delta s = \alpha(\sigma - \sigma^{\mathrm{R}})$ occurs due to the stress leakage process described by α in Eqs. (5) and (6). These slip increments are applied just after a loading update has occurred.

We continue stepping through time until $\mathrm{CFF}(\boldsymbol{x},t) \geq 0$ is established on at least one site, at which time we fix t and proceed to the stochastic slip adjustment procedure. In this procedure, we proceed in a series of parallel *monte carlo sweeps* (mcs). On the first mcs, all failing sites having the condition $\mathrm{CFF}(\boldsymbol{x},t) \geq 0$ are adjusted by a slip amount:

$$\Delta s = \frac{\{\sigma - \sigma^{\mathrm{R}}\}}{K_{\mathrm{T}}}(1+\rho) \tag{16}$$

where ρ is a random variable, typically having a uniform probability density function on the interval $(-0.1, 0.1)$, to model random overshoot or undershoot. After the initiator site(s) have been "slipped" or "failed", shear and normal stress are transferred to all other sites using the discrete form of the stress Green's functions or stress transfer coefficients $T_{ij}^{kl}(\boldsymbol{x}-\boldsymbol{x}')$. At this point, the second mcs begins, and any other site now having the stress magnitude condition $\mathrm{CFF}(\boldsymbol{x},t) \geq 0$, or the stress rate condition described by Eq. (13), fails as well, their stress is redistributed using $T_{ij}^{kl}(\boldsymbol{x}-\boldsymbol{x}')$, and so forth. In general, no healing of the segments is permitted until the end of the slip adjustment process. At the conclusion of the mcs slip adjustments, the loading process is resumed by stepping t by Δt and so on.

3. Data assimilation

Earthquake data obtained from the historical record of seismicity as well as geological field studies represent the primary physical signatures of how the earthquake cycle is affected by the frictional properties that exist on faults. The timing, magnitude and complexity of historical events are a direct reflection of the values of the frictional parameters: α, σ^{F}, σ^{R}. Since the dynamics (Eqs. (3)–(6)) depends on the characteristic length scale L for each segment, all of these frictional parameters should be regarded as scale-dependent functions of L: $\alpha = \alpha(\Delta\sigma, L)$, $\sigma^{\mathrm{F}} = \sigma^{\mathrm{F}}(L,V)$, $\sigma^{\mathrm{R}} = \sigma^{\mathrm{R}}(L,V)$. For simulations in which one or more distinct scales L are chosen for each fault segment (length and width, for example), one must choose α, σ^{F}, σ^{R} in such a way that the historical record of activity on the fault network is matched as closely as possible. This is the data assimilation problem for which we have developed a simple, but physically motivated method.

For historical earthquakes, there can be considerable uncertainty about where the event was located (Scholz,

1990). Modern studies including geologic observations (Grant and Sieh, 1994) as well as radar observations (Massonet and Feigl, 1998) of earthquakes indicate that slip or seismic moment M_o is often distributed regionally over a number of faults and sub-faults. Our technique assigns a weighted average of the scalar seismic moments for given historic or pre-historic events during an observational period to all of the faults in the system. To be physically plausible, the weighting scheme should assign most of the moment M_o to faults near the location of maximum ground shaking and decay rapidly with distance. Since the seismic moment is the torque associated with one of the moment tensor stress–traction double couples, it is most reasonable to use the (inverse cube power of distance r) law that describes the decay of stress with distance (Eshelby, 1957). Comparisons with data indicate that this method yields average recurrence intervals similar to those found in nature.

Briefly, we take the moment released by large earthquakes in the historic record over the last 200 years or so and assign it, using a $1/r_{ij}^3$ probability density function, to all of the fault segments in the system. Here $r_{ij}=|\boldsymbol{x}_i-\boldsymbol{x}_j|$ is the distance of the earthquake with epicenter at $\boldsymbol{x}_i$ to the fault segment centered at $\boldsymbol{x}_j$. This procedure leads to the assignment of an average, characteristic seismic moment to each fault segment. Once the moment is assigned, we use the slip:stress–drop relation for each rectangular fault segment, computed from the discrete equation corresponding to Eq. (6) to obtain the average stress drop at failure $\Delta\sigma_i^{\mathrm{F}}$ for the segment. Then, given a nominal normal stress across the fault segment due to gravity stresses $N_{\mathrm{g}}(\boldsymbol{x}_i)$, we compute the difference between the static and kinetic frictional coefficients $\Delta\sigma_i^{\mathrm{F}}\equiv(\mu_{\mathrm{S}}-\mu_{\mathrm{K}})_i N_{\mathrm{g}}(\boldsymbol{x}_i)$. However, in applying the slip dynamics of the model, we compute the slip needed to relieve the stress drop $\Delta\sigma_i^{\mathrm{F}}$ due to both the gravitational normal stress $N_{\mathrm{g}}(\boldsymbol{x}_i)$ as well as all elastic contributions $N_{\mathrm{e}}(\boldsymbol{x}_i)$ to the total space- and time-dependent normal stress $\chi(\boldsymbol{x}_i,t)=N_{\mathrm{g}}(\boldsymbol{x}_i)+N_{\mathrm{e}}(\boldsymbol{x}_i,t)$.

Step 1: *Assignment of moment rates.* All historical events in southern California since 1812 are used (Deng and Sykes, 1997). For each of the 650 fault segments in the model, the contribution of moment release rate from the jth historical earthquake $\mathrm{d}M_o(t_j)/\mathrm{d}t$ to the rate on the ith fault segment, $\mathrm{d}m_i/\mathrm{d}t$, is:

$$\frac{\partial m_i}{\partial t}=\frac{\sum_j \frac{\partial M_o(t_j)}{\partial t} r_{ij}^{-3}}{\sum_j r_{ij}^{-3}} \tag{17}$$

where $r_{ij}=|\boldsymbol{x}_i-\boldsymbol{x}_j|$ is the distance between the event at location $\boldsymbol{x}_j$ and time t_j, and the fault segment at $\boldsymbol{x}_i$. Application of Eq. (17) when $\boldsymbol{x}_i\approx\boldsymbol{x}_j$ is understood to be in the limiting sense. Eq. (17) arises if one regards r_{ij}^{-3} as a probability density function, and assumes that each earthquake is a point source. We correct for the largest events, which are long compared to the depth, by representing the large event as a summation of smaller events distributed along the fault.

Step 2: *Determination of friction coefficients.* The seismic moment is:

$$M_o(t_j)=\mu\langle s(t_j)\rangle A \tag{18}$$

where μ is shear modulus, $\langle s(t_j)\rangle$ is average slip at time t_j, and A is fault area. For a compact fault, the average slip in terms of stress drop $\Delta\sigma$ is (Kanamori and Anderson, 1975):

$$\langle s\rangle=\frac{f\Delta\sigma\sqrt{A}}{\mu} \tag{19}$$

where f is a dimensionless fault segment shape factor having a value typically near 1. Standard assumptions of $f\sim1$, $\Delta\sigma\sim5\times10^6$ Pa, $\mu\sim3\times10^{10}$

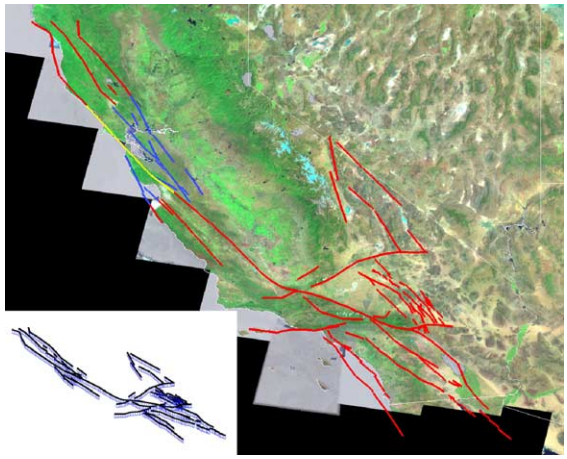

Fig. 1. Virtual California fault system of the major active strike slip faults overlain on a LandSat image of California (Figure courtesy of Peggy Li, JPL). Lines are model faults. There are 650 fault segments in the model, each capable of rupturing independently in response to plate tectonic stress acting through each segment's friction law, and each approximately 10 km in length along strike, and exactly 15 km in depth. All segments interact by means of quasi-static elasticity. The blue lines represent the "San Francisco Bay Area faults". The yellow line represents the San Andreas fault in the Bay Area region. The earthquake forecasts for future activity are computed for the blue and yellow fault segments. (Inset) Faults segments making up the Virtual California model. (For interpretation of the references to colour in this figure legend, the reader is referred to the web version of this article.)

Table 1
Table of fault data for the Virtual California model used in this paper

Fault or fault system name	Segment nos.		Chart distance (km)		Average slip rate (mm/yr)
	Begin	End	Begin	End	
Bartlett Springs	0	7	0.0	84.7	6
Calaveras	8	22	84.7	238.9	15 (8→17) 6 (18→22)
Collayomi	23	25	238.9	266.8	.6
Concord-Green Valley	26	31	266.8	322.2	6
Death Valley	32	55	322.2	569.6	5 (32→49) 4 (50→55)
Garberville-Briceland	56	59	569.6	609.2	9
Greenville	60	66	609.2	682.2	2
Hayward	67	77	682.2	793.3	9 (67→74) 3 (75→77)
Hunter Mtn.-Saline Val.	78	84	793.3	861.3	2.5
Hunting Creek-Berryessa	85	90	861.3	920.3	6
Lake Mountain	91	93	920.3	953.7	6
Maacama	94	111	953.7	1133.3	9
Monterey Bay-Tularcitos	112	119	1133.3	1213.6	.5
Ortigalita	120	126	1213.6	1280.1	1
Owens Valley	127	138	1280.1	1401.6	1.5
Palo Colorado-Sur	139	146	1401.6	1479.8	3
Panamint Valley	147	156	1479.8	1584.5	2.5
Quien Sabe	157	158	1584.5	1607.6	1
Rinconada	159	177	1607.6	1796.9	1
Rodgers Creek	178	183	1796.9	1858.9	9
Round Valley	184	189	1858.9	1914.3	6
San Gregorio	190	198	1914.3	2003.3	5
Sargent	199	203	2003.3	2056.0	3
West Napa	204	206	2056.0	2085.9	1
White Mountains	207	216	2085.9	2186.5	1
San Andreas North	217	263	2186.5	2653.6	24 (217→248) 17 (249→263)
San Andreas Creeping	264	273	2653.6	2751.3	34
San Andreas South	274	335	2751.3	3330.7	34 (274→298) 30 (299→312) 24 (313→321) 25 (322→335)
San Jacinto	336	364	3330.7	3622.1	12 (336→352) 14 (353→364)
Elsinore	365	388	3622.1	3857.5	3 (365→368) 5 (369→384) 4 (385→388)
Imperial Valley	389	406	3857.5	4020.0	30
Laguna Salada	407	416	4020.0	4118.5	4
Garlock	417	440	4118.5	4353.0	−5 (417→426) −7 (427→440)
Palos Verdes	441	447	4353.0	4428.6	3
Santa Cruz Island	448	452	4428.6	4481.9	−3
Brawley	453	457	4481.9	4533.8	25
Santa Monica	458	468	4533.8	4653.3	−3
Cleghorn	469	470	4653.3	4676.4	−3
Tunnel Ridge	471	472	4676.4	4695.6	−1.3
Helendale	473	481	4695.6	4781.7	.8
Lenwood-Lockhart	482	499	4781.7	4955.2	.8
Pipes Canyon	500	501	4955.2	4970.8	.7
Gravel Hills-Harper	502	509	4970.8	5051.2	.9
Blackwater	510	516	5051.2	5113.0	2
Camp Rock-Emerson	517	527	5113.0	5227.2	1 (517→524) .6 (525→527)
Homestead Valley	528	530	5227.2	5254.4	.6
Johnson Valley	531	536	5254.4	5320.4	.6
Calico-Hidalgo	537	549	5320.4	5455.5	1 (537) 1.7 (538) 2.6 (539→545) .6 (546→549)
Pisgah-Bullion	550	562	5455.5	5571.2	1
Mesquite Lake	563	564	5571.2	5592.2	1
Pinto Mountain	565	573	5592.2	5676.0	−1
Morongo Valley	574	574	5676.0	5690.6	−.5
Burnt Mountain	575	576	5690.6	5707.6	.6
Eureka Peak	577	578	5707.6	5725.8	.6

(*continued on next page*)

Table 1 (*continued*)

Fault or fault system name	Segment nos.		Chart distance (km)		Average slip rate (mm/yr)
	Begin	End	Begin	End	
Hollywood-Raymond	579	582	5725.8	5763.7	−1 (579→580) −.5 (581→582)
Inglewood-Rose Cyn	583	604	5763.7	5979.2	1 (583→590) 1.5 (591→604)
Coronado Bank	605	623	5979.2	6179.5	3
San Gabriel	624 1 (634→637)	637	6179.5	6310.8	3 (624→628) 2 (630→633)
Big Pine	638	644	6310.8	6379.5	−4
White Wolf	645	649	6379.5	6427.6	−5

Each fault segment is approximately 10 km in length along strike, and 15 km in depth. "Chart distance" refers to plots such as that given in Fig. 2, in which all segments are concatenated end-to-end for plotting purposes. For slip rates, positive slip rate is right lateral, negative slip rate is left lateral.

Pa yield reasonable slip values. The average slip is converted to a difference between static and kinetic friction, $(\mu_S - \mu_K)_i$, for the ith fault segment via the relation:

$$(\mu_S - \mu_K)_i \approx \frac{m_i}{fA^{3/2}\chi_i} \tag{20}$$

obtained by combining Eqs. (18), and (19), m_i is the individual fault patch moment, and $\Delta\sigma \approx \sigma^F - \sigma^R$. To compute $(\mu_S - \mu_K)_i$, a typical value of χ_i for each segment is computed from the average gravitationally induced compressive stress. Since the stochastic nature of the dynamics depends only on the differences $(\mu_S - \mu_K)_i$ (Rundle, 1988; Rundle et al., 2001), we set $\mu_K = .001$ (all i).

Step 3, the assignment of the aseismic slip factors α_i has been discussed above.

4. Results

4.1. Fault model

The fault model we use in the Virtual California simulations described here is shown in Fig. 1. The colored lines represent the fault model, and the inset shows a perspective view of the 650 segments that comprise the model. The geometry of most of southern California is primarily based on Table 2 of Deng and Sykes, 1997, which contains southern California faults that are recognized to have slip rates of at least 3 mm/yr. The faults are split into individual, straight segments. Other fault parameters were taken from the table of values compiled by *Barnhard and Hanson* for the USGS 1996 Hazard Maps.[12] Table 1 shows the faults that are used in the model, and identifies the segments associated with them. Note that all fault segments in the model extend from the surface to 15 km depth, and all are approximately 10 km in length along strike as described above. Thus the model is both three-dimensional and elastic, as it is contained fully in the upper crust. Slip on the segments is constant over each segment, but depth dependent slip will be examined in future models currently under development.

In the results presented below, the failure physics conforms with Eqs. (6) and (13), in which dynamic fracture weakening is used for all faults in the model. In another publication (Rundle et al., 2004), we have examined another type of failure physics in which dynamic weakening was only allowed on the San Andreas fault proper, but the differences between the two types of models were not found to be significant. Note that all 650 interacting fault segments are present, the CFF$(\boldsymbol{x},t)=0$ failure physics, and the α-stress leakage effect are operative. We also take $\alpha \approx .1/T_B$ for most fault segments, where T_B is the recurrence interval that would be observed on the individual 10×15 km fault segment if it were in isolation (i.e., not interacting with other faults):

$$T_B \equiv \frac{\sigma^F - \sigma^R}{VK_T} \tag{21}$$

Here K_T represents the diagonal (self-interaction) term for the shear stress Green's function in the discrete representation, and $\sigma^F \equiv \mu_S N_g$, $\sigma^R \equiv \mu_K N_g$. The exception is that $\alpha \approx .45/T_B$ for the northern branch of the San Andreas fault, where we have found that the geometric complexity of the model seems to inhibit the occurrence of the large earthquakes that are observed to occur there in nature. Thus we have included this value of α as a "proxy" for more detailed physics that are as yet unidentified to encourage smoothing of the stress field on the main branch of the San Andreas, so that

[12] US Geological Survey earthquake fault data http://geohazards.cr.usgs.gov/eq/faults/fsrpage01.html.

large earthquakes are produced. We anticipate that further studies will be needed on this and other issues to resolve a number of similar open questions.

Although the "bare" values of $T_{B,i}$ can be regarded as an input to the simulation, the actual or "dressed" or "renormalized" values of $T_{R,i}$ can be expected to be different. The difference is a result of the interactions among segments, leading to the fact that the process of shear stress buildup and release will not be simply periodic, and the fact that the total normal stress $\chi(\boldsymbol{x}_i,t)=N_g(\boldsymbol{x}_i)+N_e(\boldsymbol{x}_i,t)$ has a time- and space-dependent component. Fig. 2a is a plot of both the bare $T_{B,i}$ and renormalized values of $T_{R,i}$ for all the segments. It can be seen that the renormalized values of $T_{R,i}$ are all larger (longer time intervals) than the bare values. Again, the values of $T_{R,i}$ are plotted as a function of "chart distance" of the segment (Table 1)). To date, we have not been able to calculate the renormalized values using theoretical arguments. Fig. 2b is a plot of the variability of the recurrence intervals for the segments expressed as the observed coefficient of variation (CoV) on the segments:

$$CoV \equiv \frac{\theta_i}{T_{R,i}} \tag{22}$$

where θ_i is the standard deviation for recurrence of earthquake slip on a segment. Values observed are of the order of .2–.4, which are similar to values observed world-wide on geologic faults (see the compilation of data in WGCEP, 2003).

An example of the Coulomb Failure Function stress $CFF(\boldsymbol{x},t)$ as defined in Eq. (9) is shown for a typical simulation. The ordinate is time in years, and the abscissa is the "chart distance" (see Table 1) of each individual segment. The figure is essentially a space–time snapshot of the dynamics. Horizontal lines represent earthquakes, and the buildup and release of $CFF(\boldsymbol{x},t)$ during the earthquake cycle can be seen in space and time. Darker colors represent lower $CFF(\boldsymbol{x},t)$, and lighter colors represent higher $CFF(\boldsymbol{x},t)$. Note the development of a stress shadow in the eastern Mojave (right-facing arrow), represented by a lower stress level, as the result of the occurrence of a large earthquake on the southern San Andreas (left-facing arrow).

Two examples of typical large earthquakes on the northern and southern San Andreas fault are shown in Figs. 3 and 4. Note particularly that the segments participating in the event are not entirely contiguous, but that there are smaller, discontinuous groups of slipped segments participating in the event as well. The epicentral segment is shown as a darker rectangle in both figures. This type of non-compact, discontinuous slip has been seen in real earthquakes as well, for example in InSAR observations of earthquake displacements (e.g., Massonet and Feigl, 1998).

4.2. Statistics

Fig. 5 shows the magnitude–frequency statistics for the simulation. The magnitude m is defined in terms of

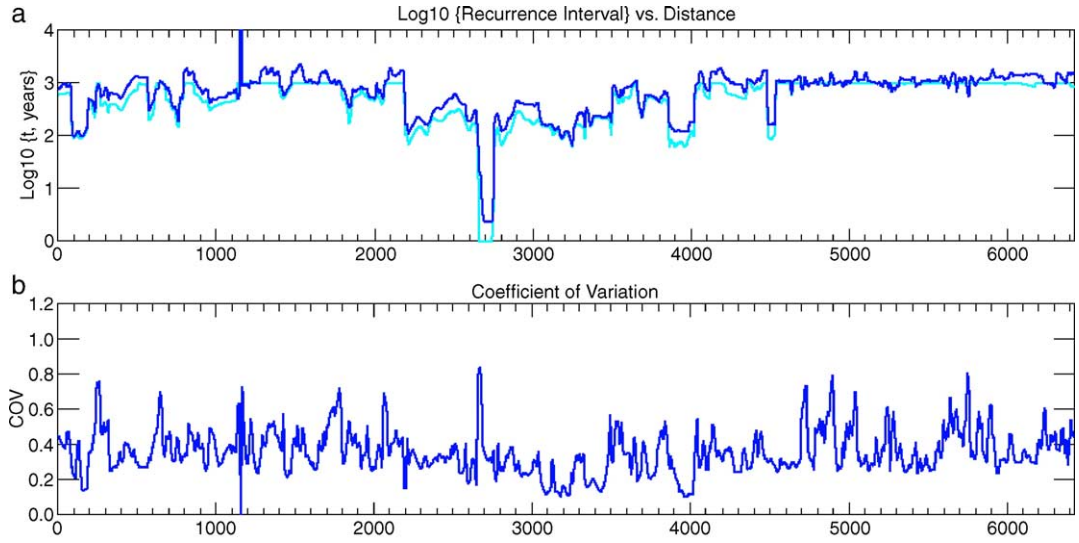

Fig. 2. (a) Plot showing both (input) "bare" recurrence intervals, and (output) "dressed" or "renormalized" recurrence intervals for a typical simulation. The bare recurrence intervals are shorter than (smaller than) the renormalized intervals. The input recurrence intervals differ from the output intervals due to the effects of elastic interactions. (b) Plot of the average coefficient of variation for the simulation as a function of (chart) distance along the fault system. See Table 1 for identification of chart distance with fault locations and fault segment locations.

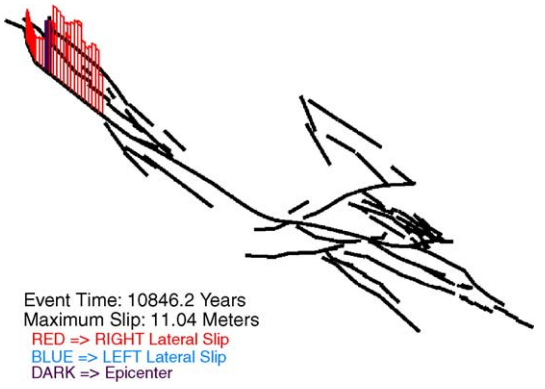

Fig. 3. Example of a large event on the northern San Andreas fault. The epicentral segment is shown in dark. Slip in this event occurs not only on the San Andreas fault proper, but also on other sub-parallel faults. The non-contiguous segments that slip are directly associated with the earthquake, and can be also be regarded as "aftershocks". Maximum slip in this event is 11.04 m.

the seismic moment M in our simulations similar to Eq. (18):

$$M = \mu \int s(\boldsymbol{x}, t)\mathrm{d}\boldsymbol{x} \tag{23}$$

$$m = \frac{2}{3}\log_{10} M - 6.0 \tag{24}$$

where $s(\boldsymbol{x},t)$ is the slip at $\boldsymbol{x}$ at time t, μ is the shear modulus, and the integral is taken over all fault segments that slipped in the event at time t. The constant 6.0 is appropriate for variables in SI units.

It should be noticed first that the form of the magnitude–frequency statistics is similar to the Gutenberg–Richter (GR) relation, in that there appears to be an interval in that can be approximated by a straight line having a slope of approximately 1. However, the data are not well-represented by a straight line over the entire interval, and the data are sharply truncated at the lower end due to the minimum scale of fault segments in the model. The area of these segments is approximately 10 km (length) × 15 km (depth), corresponding roughly to a m~6 earthquake. It is for that reason that a breakdown in scaling at about the m~6 level is seen in Fig. 5. At the other end, a cutoff of events is seen about m~8, similar to observations in nature. Note that there is a dashed line of slope = 1 drawn in the range between $6.5 < m < 7.5$ for comparison with the points. Gutenberg–Richter b-values determined by fits to the curves corresponding to each symbol are given on the figure, and all are near the observed value of b~1.

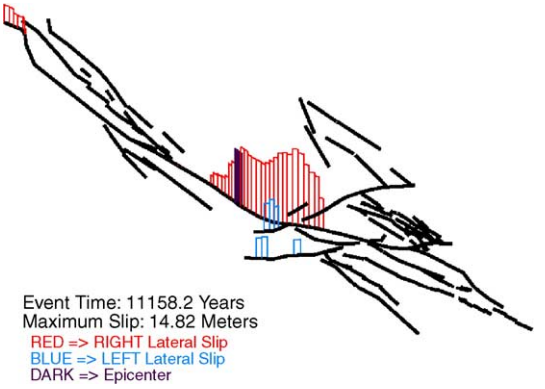

Fig. 4. Example of a large event on the southern San Andreas. The epicentral segment is shown in dark. Again, it can be seen that slip occurs not only on the San Andreas fault proper, but also on other non-contiguous fault segments. Maximum slip in this event is 14.82 m.

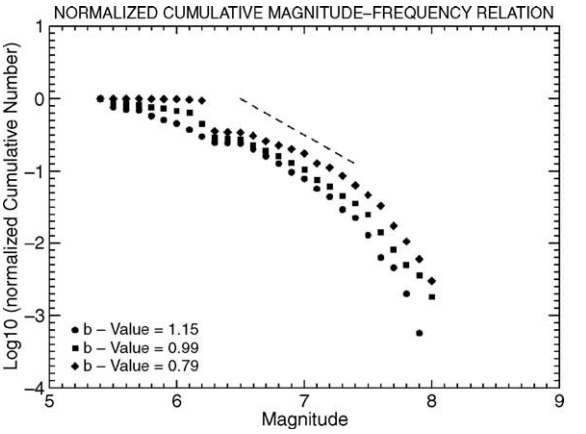

Fig. 5. Three examples of normalized Gutenberg–Richter curves. Dashed line has slope −1 and is drawn in the interval $6.5 < m < 7.5$. b-values shown are the result of fits to the points in the same interval. Different points correspond to different values of η. Refer to Eq. (13), and set $\gamma \equiv \frac{\eta \Delta t}{\Delta \sigma^2}$. Then the different points correspond to $\gamma = 1$ (circles), .75 (squares), .5 (diamonds).

The various GR curves are all normalized, i.e., we plot the cumulative number $N(>m)/N(>-\infty)$. In Fig. 5, different points correspond to different values of γ and therefore η. Referring to Eq. (13), the different point-curves correspond to: $\eta = 1$ (circles, 3488 events); $\eta = .75$ (squares, 2216 events); and $\eta = .5$ (diamonds, 1330 events). These numbers confirm the obvious conclusion that the physics corresponding to dynamic weakening with $\eta < 1$ allows small earthquakes to grow into larger earthquakes more easily than for $\eta = 1$. It can be easily seen that smaller values of η lead to significant increases in the number of large earthquakes, with a corresponding depletion in the number of smaller earthquakes.

5. Ensemble forecasting

The report from the Working Group on California Earthquake Probabilities (WGCEP, 2003) represents the latest version of a method that has been developed for using observed geological and geophysical data, together with broad assumptions about the appropriate statistical distribution functions that describe the stochastic nature of the process. In the WGCEP (2003) method, the models that are used to compute a forecast from the data are statistical in nature, that is, the physics included is typically encoded in 1) the form of the statistical distribution, and 2) the parameters of the distribution, usually the mean and variance. WGCEP then uses the statistical distribution for all the fault segments in a region, with means and variances set using the geological and geophysical data, to compute the conditional probability that a large ($m \geq 6.7$) event will occur in the San Francisco Bay region during the period 2002–2031, given that the last such event occurred a time T years ago.

In our approach, we use our Virtual California simulations to generate ("measure") the statistical distribution needed to compute the conditional probability. The basic idea is to use the essentially the same data sources and presumably fault model as the WGCEP group, but to replace the assumptions made about the form of the statistical distribution with measurements of the statistics of earthquake occurrence on the faults of interest that are obtained from our simulations.

The primary statistical distributions investigated by the WGCEP are the Lognormal distribution (e.g., Evans et al., 1993), and the Brownian first passage, or Brownian Passage Time (BPT) distribution (Rangarajan and Ding, 2000; Matthews et al., 2002). The Lognormal distribution is known to describe a number of physical situations where ageing, fatigue, and failure processes occur. Then the probability density function (PDF) for failure between time t and $t+\delta t$ is given by:

$$P_{\mathrm{LN}}(t) = \frac{1}{\theta t\sqrt{2\pi}} \exp\left\{ \frac{-[\log(t/\lambda)]^2}{2\theta^2} \right\} \tag{25}$$

where $\log\lambda$ is the central value (mean) for the density function, and θ is the geometric standard deviation.[13]

Likewise, the Brownian Passage Time PDF for failure between time t and $t+\Delta t$ is given by (Rangarajan and Ding, 2000; Matthews et al., 2002):

$$P_{\mathrm{BPT}}(t) = \sqrt{\frac{\lambda^3}{2\pi\theta^2 t^3}} \exp\left\{ -\frac{\lambda(t-\lambda)^2}{2\theta^2 t} \right\} \tag{26}$$

[13] Log Normal distribution: http://www.asp.ucar.edu/colloquium/1992/notes/part1/node105.html, see also: http:/MathML:/mathworld.wolfram.com/LogNormalDistribution.html.

In the WGCEP method, the values for the standard deviation of earthquake recurrence time θ_i, and the mean recurrence time interval λ_i are inferred from a variety of observations on the selected Bay Area fault segments. A problem that is sometimes encountered is that for some segments, observations for only the last earthquake involving that segment exist,[7] thus the values of θ_i and λ_i are estimated by indirect means. Once the PDFs $P(t)$ for the segments are established, the Cumulative Distribution Function $C(t)$, also called simply the "distribution function", is then used to compute the conditional probability (also called the "discrete hazard function") for failure of the segment during the interval $(T, T+\Delta T)$, given that it has been a time T since the last such failure (WGCEP, 2003; see Footnote 14):

$$P(T \leq t \leq T+\Delta T | tT) = \frac{C(T+\Delta T) - C(T)}{1 - C(T)} \tag{27}$$

The WGCEP (2003) computes the $\Delta T = 30$ year conditional probabilities (Eq. (27)) for the interval 2002–2031, for the occurrence of an earthquake with magnitude $m \geq 6.7$, occurring on the active earthquake faults in the San Francisco Bay region. Using a variety of PDFs, including the Lognormal and the BPT distributions, they find a 62% probability during the time period 2002–2031.

We can perform a similar forecast calculation for essentially the same group of San Francisco Bay area faults using Virtual California, but instead of assuming the PDF $P(t)$ and its associated distribution $C(t)$, we can measure these quantities from simulations. Our method uses basically the same observational data as does the WGCEP, but instead of using these data to estimate the statistical parameters θ_i and λ_i for each fault segment, the data are assimilated into physical values for the Virtual California fault segments as described above. We then use the simulations to directly measure $P(t)$ and $C(t)$, for the fault segments of interest, then compute $P(T \leq t \leq T+\Delta T | t \geq T)$ as in Eq. (27).

The result of our computations is shown in Fig. 6. Fig. 6a shows the measured histogram of intervals between successive earthquakes having $m \geq 6.7$, occurring on the San Francisco Bay area faults (blue fault segments together with yellow fault segment in Fig. 1) for 40,000 years of simulated earthquakes. When properly normalized, the histogram can be used as a PDF. Also shown on Fig. 6a are both the Lognormal distribution (solid line) and the BPT distribution (dashed line) having the same overall mean λ and standard

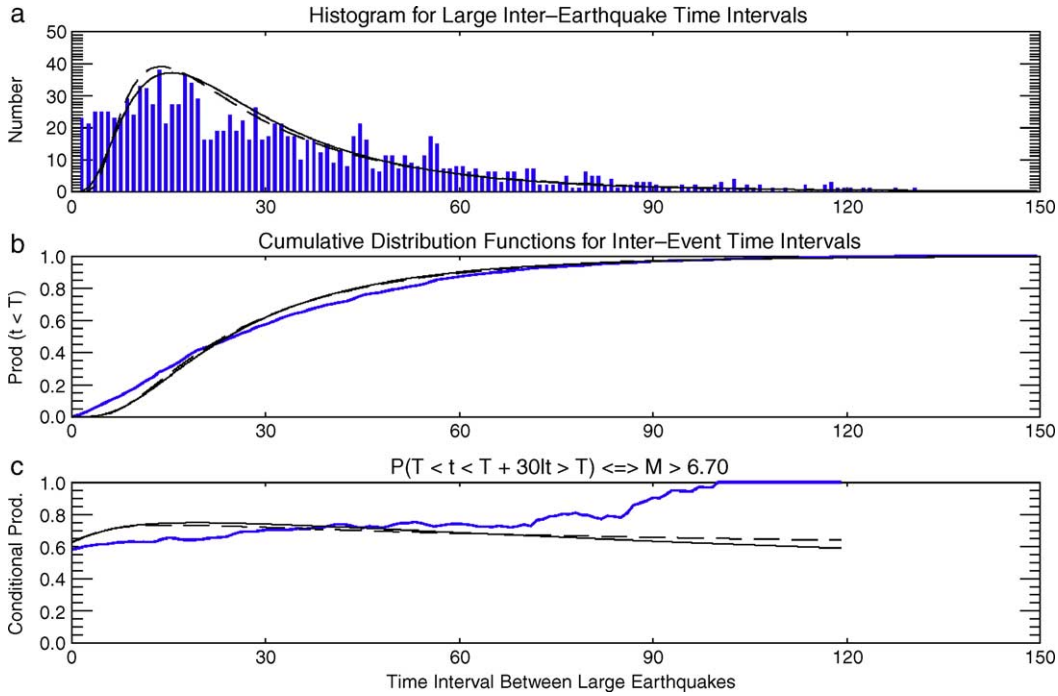

Fig. 6. (a) Histogram for time intervals between large earthquakes having $m \geq 6.7$ on the San Francisco Bay area faults, which are shown in Fig. 1 in blue and yellow. Also shown are the Lognormal (solid line) and Brownian Passage Time distributions (dashed line) having the same mean and variance as the simulation data in the histogram. All curves are normalized to the same value. (b) (Cumulative) distribution functions corresponding to (a). (c) Conditional probabilities $P(T \leq t \leq T+30 \text{ years} | t \geq T)$, also called 30-year discrete hazard functions, corresponding to the distributions in (b).

deviation θ as the measured histogram simulation data. Fig. 6b shows the associated distribution function (thick blue line) corresponding to the histogram of simulation data, together with the distribution functions for the Lognormal distribution (solid line) and the BPT distribution (dashed line). Fig. 6c shows the conditional probabilities $P(T \leq t \leq T+30 \text{ years} | t \geq T)$ for the simulation data (thick blue line), the Lognormal distribution (solid line), and the BPT distribution (dashed line).

As can be seen from Fig. 6, the PDF and the conditional probabilities measured from simulations are different than the same functions arising from the Lognormal and BPT distributions. The greatest difference is shown by the 30-year conditional probability (discrete hazard function), where the Lognormal curve decreases with time after a just a few years, and the BPT curve rises initially, then remains approximately constant. By contrast, the hazard function arising from simulations rises nearly monotonically from a value of about 59% at time interval $T=0$ to a value of 1 at about $T=100$ years. The hazard function from the simulations tells us that the longer the time interval during which a large earthquake has not occurred, the greater probability that it will occur during the ensuing 30 years.

Finally, we can use Fig. 6c to evaluate the probability of an $m \geq 6.7$ event in the San Francisco Bay area on one of the major faults shown in Fig. 1. We note that the Loma Prieta earthquake occurred in 1989, and we consider that it occurred on one of the San Francisco Bay faults including the San Andreas fault (see WGCEP, 2003, for a discussion of the Loma Prieta earthquake). Using Fig. 6c, it can be seen that as of 2003, the initial time of the *WGCEP* forecast, the probability of an $m \geq 6.7$ occurring 14 years after the $m=6.9$ Loma Prieta earthquake is 65%, in general agreement with the WGCEP (2003) value of 62%.

An important caveat to note is that with the Virtual California simulations, we can only forecast large earthquakes that occur on the faults in the model. It is possible that large earthquakes may occur on faults not included in the model, for example blind thrust faults or relatively inactive strike slip faults; therefore our 30-year estimate of 65% of the probability of a large $m \geq 6.7$ earthquake in the San Francisco Bay region must be regarded as a lower bound.

6. Final comments and discussion

We have described the model underlying the simulation code *Virtual California*, which is a fully three-dimensional, interacting, laboratory friction-based, backslip-loaded model for the earthquake activity on

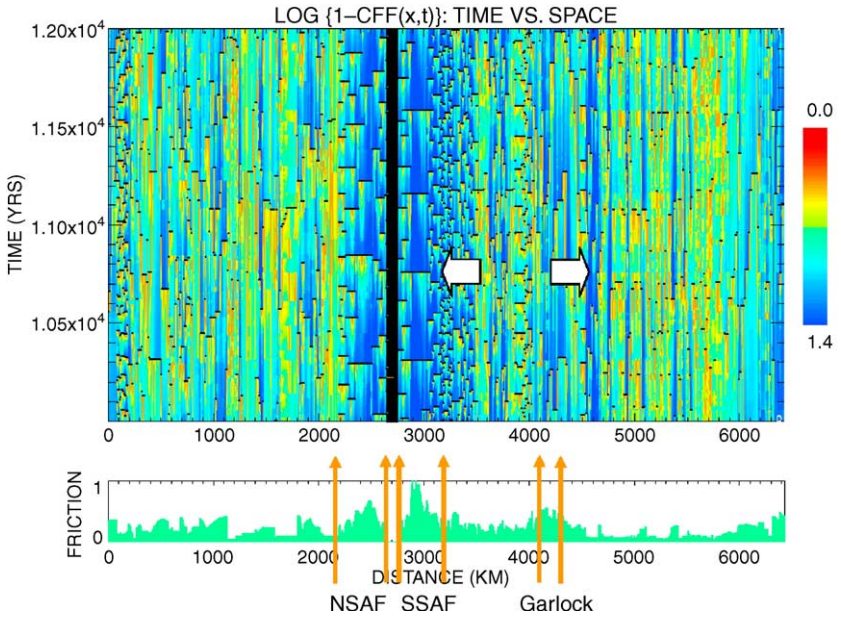

Fig. 7. Plot of Coulomb Failure Function for a time interval of 1000 years for a typical model run. Specifically, color contours of the function $\log_{10}\{1-\mathrm{CFF}(\boldsymbol{x},t)\}$ are plotted as a function of chart distance (see Table 1). Cool colors (low CFF stress, farther from failure) represent larger values of $|\mathrm{CFF}(\boldsymbol{x},t)|$, and hotter colors represent smaller values (high CFF stress, closer to failure). Time is along the vertical axis and chart distance is along the horizontal axis. The bottom histogram ("Friction") is a plot of the difference between static and kinetic, or dynamic friction coefficients, $\mu_S-\mu_K$, as a function of (chart) distance in km. Stress shadow (decrease of CFF stress) on faults of the Eastern Mojave can be seen (right white arrow) in response to earthquake on southern San Andreas fault (left white arrow). Note, also, small stress increases, or enhancements, that can be seen as jumps in the stress level at a number of locations at the same time.

the major strike slip fault systems of California. We have described the equations and their physical justification, and we have furthermore outlined the basic data assimilation procedure that we used to set the large number of parameters in the model. Future work will be needed to refine these equations and data assimilation methods using Kalman Filters or other methods to develop a method to update model parameters as new data are acquired, a process called "model steering".

We find that our simulations produce realistic statistical distributions of activity on the faults in the model. The largest earthquakes are similar in area extent and slip amplitude to the corresponding quantities from observations of actual great California earthquakes, and other statistics such as recurrence intervals, coefficients of variation, and general characteristics of the magnitude–frequency statistics are similar to observed data as well. However, there is clearly need for improvement, and future work will be directed at quantifying the degree of improvement possible, as well as developing the techniques needed for better data assimilation and model steering procedures.

Our work shows the importance of interactions, and how these lead to the emergence of correlations in earthquake activity. Our simulations predict that stress shadows and stress enhancements are a direct result of the elastic interactions present in the earth (Fig. 7). Furthermore, we find that our simulations can be developed into methods to forecast future activity using current and newly developed simulation-based procedures (Rundle et al., 2004), which will be discussed in future work.

A final point we discuss concerns a lively debate[14] focusing on the question posed by Davis et al. (1989) in the context of earthquake forecasting models:

> (is it true that) "The longer it has been since the last earthquake, the longer the expected time till the next?"

A series of papers considered this question, notably Sornette and Knopoff (1997), Ward and Goes (1993) and Goes and Ward (1994). The conclusion was that the answer depended strongly on which PDF was used to model the aging and failure process. For example, the Lognormal distribution has the property that, after an initial short time period, the longer the time interval since failure, the lower the probability of failure. This

[14] *Nature* debate on earthquake forecasting 1999: http://www.nature.com/nature/debates/earthquake/equake/frameset.html.

property can clearly be seen in Fig. 6, and is quite different from the probability of failure associated with the Virtual California simulation. In the latter, the probability of a large earthquake on the San Francisco Bay area faults rises with the time interval since the last large event, nearly monotonically in time. The basic reason for this difference is that every fault in Virtual California fails eventually, because the model fluctuates around a steady state of accommodation to the driving plate motion. Therefore, in our simulations it is not possible for some group of faults to fail once and then never fail again, which is the basic reason why some PDFs produce a positive answer to the Davis et al. (1989) question.

Acknowledgements

This work has been supported by a grant from US Department of Energy, Office of Basic Energy Sciences to the University of California, Davis DE-FG03-95ER14499 (JBR); with additional funding from the National Aeronautics and Space Administration under grants to the Jet Propulsion Laboratory and the University of California, Davis (JBR; PBR, GM, DT; AD, PL). This research was also supported in part by the Southern California Earthquake Center (PBR). SCEC is funded by NSF Cooperative Agreement EAR-0106924 and by USGS Cooperative Agreement 02HQAG0008. SCEC contribution number for this paper is 777.

References

Achuta Rao, K., Sperber, K.R., 2002. Simulation of the El Nino Southern Oscillation: results from the Coupled Model Intercomparison Project. Clim. Dyn. 19, 191–209.

Covey, C., AchutaRao, C.M., Cubasch, U., Jones, P., Lambert, S.J., Mann, M.E., Phillips, T.J., Taylor, K.E., 2003. An overview of results from the Coupled Model Intercomparison Project. Glob. Planet. Change 37, 103–133.

Crampin, S., Chastin, S., 2003. A review of shear wave splitting in the crack-critical crust. Geophys. J. Int. 155, 221–240.

Crampin, S., Peacock, S., 2005. A review of shear-wave splitting in the compliant crack-critical anisotropic earth. Wave Motion 41, 59–77.

Davis, P.M., Jackson, D.D., Kagan, Y.Y., 1989. The longer it has been since the last earthquake, the longer the expected time till the next? Bull. Seism. Soc. Am. 79, 1439–1456.

Deng, J.S., Sykes, L.R., 1997. Evolution of the stress field in southern California and triggering of moderate sized earthquakes: a 200-year perspective. J. Geophys. Res. 102, 9859–9886.

Eshelby, J.D., 1957. Proc. R. Soc. Lond. Ser. A 241, 376.

Evans, M., Hastings, N., Peacock, B., 1993. Statistical Distributions. Wiley Interscience, New York.

Freund, L.B., 1990. Dynamic Fracture Mechanics. Cambridge University Press, Cambridge, UK.

Gabrielov, A., Newman, W.I., Knopoff, L., 1994. Lattice models of failure — sensitivity to the local dynamics. Phys. Rev., E 50, 188–197.

Goes, S.D.B., Ward, S.N., 1994. Synthetic seismicity for the San Andreas fault. Ann. Geof. 37, 1495–1513.

Grant, L.B., Sieh, K., 1994. J. Geophys. Res 99, 6819.

Hashimoto, M., 2001. Complexity in the recurrence of large earthquakes in southwest Japan: a simulation with an interacting fault system model. Earth, Planets Space 52, 249–259.

Hashimoto, C., Matsu'ura, M., 2002. 3-D simulation of earthquake generation cycles and evolution of fault constitutive properties. Pure Appl. Geophys 159, 2175–2199.

Hergarten, S., 2002. Self-Organized Critically in Earth Systems. Springer-Verlag, Berlin.

Kanamori, H., Anderson, D.L., 1975. Bull. Seism. Soc. Am 65, 1073.

Kanninen, M.F., Popelar, C.H., 1985. Advanced fracture mechanics. Oxford Engineering Series vol. 15. Oxford University Press, New York.

Karner, S.L., Marone, C., 2000. Effects of loading rate and normal stress on stress drop and stick–slip recurrence interval. In: Rundle, J.B., Turcotte, D.L., Klein, W. (Eds.), Geocomplexity and the Physics of Earthquakes, Geophysical Monograph vol. 120. American Geophysical Union, Washington, D.C., pp. 187–198.

Kravtsov, Y.A., Kadtke, J.B. (Eds.), 1996. Predictability of Complex Dynamical Systems. Springer-Verlag, Berlin, Germany.

Matsu'ura, M., Nakajima, K., Mora, P. (Eds.), 2001. Proceedings of the 2nd ACES Workshop. Published by. APEC Cooperation for Earthquake Simulation, Brisbane, Queensland, AU.

Matthews, M.V., Ellsworth, W.L., Reasenberg, P.A., 2002. A Brownian model for recurrent earthquakes. Bull. Seism Soc. Am. 92, 2233–2250.

Massonet, D., Feigl, K.L., 1998. Rev. Geophys. 36, 441.

Mora, P. (Ed.), 1999. Proceedings of the 1st ACES Workshop. Published by. APEC Cooperation for Earthquake Simulation, Brisbane, Queensland, AU.

Mulargia, F., 1997. Retrospective validation of the time association of precursors. Geophys. J. Int. 131, 500–504.

Mulargia, F., 2001. Retrospective selection bias (or the benefit of hindsight). Geophys. J. Int. 146, 489–496.

Mulargia, F., 2004. Earthquakes as a three stage process. Geophys. J. Int. 158, 98–108.

Mulargia, F., Tinti, S., 1985. Seismic sample areas defined from incomplete catalogs — an application to the Italian territory. Phys. Earth Planet. Int. 40, 273–300.

Preston, E.L., 2001. Abelian fault models, Ph.D. dissertation, University of Colorado.

Preston, E.F., Martins, J.S.S., Rundle, J.B., 2005. Simulated dynamical weakening and Abelian avalanches in mean-field threshold systems. Physica, A 348, 572–590.

Rabinowicz, E., 1995. Friction and Wear of Materials. (2nd ed.) John Wiley, New York.

Rangarajan, G., Ding, M., 2000. First passage time problem for biased continuous-time random walks. Fractals 8, 139–145.

Rundle, J.B., 1988. A physical model for earthquakes, 2. Application to southern California. J. Geophys. Res. 93, 6255–6274.

Rundle, J.B., Turcotte, D.L., Klein, W. (Eds.), 2000a. Geocomplexity and the Physics of Earthquakes, Geophysical Monograph vol. 120. American Geophysical Union, Washington, DC.

Rundle, P.B., Rundle, J.B., Tiampo, K.F., Martins, J.S.S., McGinnis, S., Klein, W., 2000b. Triggering dynamics on earthquake fault networks. In: Bokelmann, G., Kovach, R.L. (Eds.), Proc. 3rd

Conf. Tectonic Problems of the San Andreas Fault System, Stanford U. Publ., Geol. Sci. vol. XXI. pp. 305–317.

Rundle, P.B., Rundle, J.B., Tiampo, K.F., Martins, J.S.S., McGinnis, S., Klein, W., 2001. Nonlinear network dynamics on earthquake fault systems. Phys. Rev. Lett. 87 (148501), 1–4.

Rundle, J.B., Turcotte, D.L., Sammis, C., Klein, W., Shcherbakov, R., 2003. Statistical physics approach to understanding the multiscale dynamics of earthquake fault systems (invited). Rev. Geophys. Space Phys. 41 (4). doi:10.1029/2003RG000135.

Rundle, J.B., Rundle, P.B., Donnellan, A., Fox, G.C., 2004. Gutenberg–Richter statistics in topologically realistic system-level earthquake stress-evolution simulations, Earth Planets Space 56, 761–771.

Saxena, A., 1998. Nonlinear Fracture Mechanics for Engineers. CRC Press, Boca Raton, FL.

Scholz, C.H., 1990. The Mechanics of Earthquakes and Faulting. Cambridge University Press, Cambridge, UK.

Sornette, D., Knopoff, L., 1997. The paradox of the expected time until the next earthquake. Bull. Seism. Soc. Am. 87, 789–798.

Tullis, T.E., 1996. Rock friction and its implications for earthquake prediction examined via models of Parkfield earthquakes. Proc. Natl. Acad. Sci. U. S. A. 93, 3803–3810.

Turcotte, D.L., 1991. Earthquake prediction. Annu. Rev. Earth Planet. Sci. 19, 263–281.

Ward, S.N., 1996. A synthetic seismicity model for southern California: cycles, probabilities and hazard. J. Geophys. Res. 101.

Ward, S.N., 2000. San Francisco bay area earthquake simulations, a step towards a standard physical model. Bull. Seism. Soc. Am. 90, 370–386.

Ward, S.N., Goes, S.D.B., 1993. How regularly do earthquakes recur? A synthetic seismicity model for the San Andreas fault. Geophys. Res. Lett. 20, 2131–2134.

WGCEP (Working Group on California Earthquake Probabilities), Earthquake probabilities in the San Francisco Bay region, US Geol. Survey Open File Report 03-214, US Geological Survey (2003) (see also Footnote 7).

Zoback, M.L., 1992. 1st-order and 2nd-order patterns of stress in the lithosphere — the World Stress Map project. J. Geophys. Res. 97, 11703–11728.